Journal of Cleaner Production 318 (2021) 128513

Contents lists available at ScienceDirect

Journal of Cleaner Production

journal homepage: www.elsevier.com/locate/jclepro

Metal organic framework decorated with molybdenum disulfide for visible-light-driven reduction of hexavalent chromium: Performance and mechanism

Wen-Qiang Li [a], Yi-Xuan Wang [a], Yuan-Ming Li [b], Chuan-Shu He [a,c,*], Bo Lai [c], Fei Chen [a], Hui-Juan Wang [d], Xiao-Guo Zhou [b], Yang Mu [a,**]

[a] CAS Key Laboratory of Urban Pollutant Conversion, Department of Environmental Science and Engineering, University of Science and Technology of China, Hefei, China
[b] Department of Chemical Physics, University of Science and Technology of China, Hefei, 230026, China
[c] Sino-German Centre for Water and Health Research, Sichuan University, Chengdu, 610065, China
[d] Experimental Center of Engineering and Material Science, University of Science and Technology of China, Hefei, 230026, China

ARTICLE INFO

Handling editor: Prof. Jiri Jaromir Klemeš

Keywords:
Metal organic framework
Molybdenum disulfide
Photoreduction
Heterojunction
Transient absorption spectroscopy

ABSTRACT

This work demonstrates that the photoreduction of hexavalent chromium using iron-based metal organic framework was able to be enhanced through doping molybdenum disulfide. The 1.5 wt % molybdenum disulfide doped iron-based metal organic framework exhibited the best photocatalytic activity towards hexavalent chromium reduction with an efficiency of 98.8% over 60 min, accompanied by remarkable repeatability and stability. The enhancement of photocatalytic efficiency could be achieved by (i) relieving the recombination process of photogenerated carriers in iron-based metal organic framework resulting from the formation of heterojunction, (ii) reducing photogenerated electrons transfer resistance from the interior to the surface of iron-based metal organic framework because of favorable electron transfer of molybdenum disulfide, and (iii) regulating the positive charge distribution on the surface of iron-based metal organic framework. Importantly, nanosecond time-resolved transient absorption spectroscopy further disclosed that the doping of molybdenum disulfide fundamentally improved the utilization of photogenerated electrons. This work evidences the important role of heterojunction from a microscopic perspective, which provides inspiration for the preparation of highly-efficient environmental functional photocatalysts based on iron-based metal organic frameworks.

1. Introduction

Heavy metal contamination has threatened the ecological environment security and even the human health with the rapid industrialization and urbanization process. Chromium, as a representative heavy metal element commonly utilized in industrial process such as electroplating, chemical industry and metallurgy manufacturing, has been detected at high levels in many natural water bodies due to the continuous spread of human footsteps. The main forms of chromium in nature are hexavalent chromium (Cr(VI)) and trivalent chromium (Cr(III)) according to the difference of environmental stability (de Bittencourt et al., 2020). Cr(III) is almost innocuous and plays an important role in the metabolism of animals and plants at trace level (Borthakur et al., 2019), whereas Cr(VI) is a carcinogen, mutagen and teratogen. Therefore, reduction of aqueous Cr(VI) into Cr(III) has become a favorable strategy to effectively treat Cr(VI) contamination (Wang et al., 2021). It is generally acknowledged that bioremediation, chemical treatment and photoreduction constitute the main pathways to achieve Cr(VI) reduction. Among these, photoreduction method has the advantages of short time-consuming and less secondary pollution (Shi et al., 2015; Du et al., 2019; Li et al., 2018) in contrast with sluggish biological reduction and high-cost chemical reduction. This process typically relies on the electron-hole pairs generated in the photocatalyst under light irradiation, the electrons which subsequently migrate to the

* Corresponding author. CAS Key Laboratory of Urban Pollutant Conversion, Department of Environmental Science and Engineering, University of Science and Technology of China, Hefei, China.
** Corresponding author.
E-mail addresses: hecs@scu.edu.cn (C.-S. He), yangmu@ustc.edu.cn (Y. Mu).

https://doi.org/10.1016/j.jclepro.2021.128513
Received 22 January 2021; Received in revised form 28 June 2021; Accepted 29 July 2021
Available online 31 July 2021

photocatalyst surface are capable of reducing Cr(VI) to Cr(III) in the solution (Shi et al., 2015).

Metal organic framework (MOF), as an emerging multifunctional crystalline material with tunable porosity and surface area, has occupied research hotspots in the past few decades (Trickett et al., 2019). The versatility in the compositions of metal cluster and organic ligand allows rational design via a diverse class of methodologies to control their photocatalytic activity (Zhang and Park, 2019). Typically, iron-based MOFs (Fe-MOFs) have been widely studied to explore the feasibility of their application in Cr(VI) removal because of its environmental-friendly behavior and good stability in aqueous solution (Springthorpe et al., 2019; Shi et al., 2015; Zhao et al., 2017). For instance, Fe-MOFs comprising Fe_3-μ_3-oxo clusters were reported to be used as an efficient photocatalyst for Cr(VI) photoreduction driven by visible light (Laurier et al., 2013). Fe-MOF materials assembled by amino-functionalized ligands with iron salts was found to be capable of faster removing aqueous Cr(VI) under visible light illumination (Shi et al., 2015). Unfortunately, the intrinsic defects, such as poor carrier separation efficiency and low electron conductivity, limit the application of Fe-MOFs in Cr(VI) photoreduction (Sheberla et al., 2017).

Efforts are always being dedicated to enhancing the photoreduction efficiency of Cr(VI) using Fe-MOFs by introducing various semiconductors. Among them, construction of heterojunction by coupling metal oxides with Fe-MOFs to improve the photoreduction performance is a common strategy (Oladipo et al., 2018; Wang et al., 2020; Yuan et al., 2019). Nevertheless, the intrinsic wide band gap distribution of metal oxides usually makes them less sensitive to visible light and the slow electron conduction capacity also greatly restricts the utilization of photogenerated electrons. MoS_2, as a flake-like two-dimensional material, exhibits extended light absorption range and excellent electrical conductivity. Moreover, the well-defined proper band gap and band-edge potential of MoS_2 made it more conductive to construct heterojunction with MOF photocatalysts for the enhancement of hydrogen evolution (Subudhi et al., 2020; Nguyen et al., 2018; Hao et al., 2017), while remains unexplored for Cr(VI) reduction. On the other hand, it should be noted that the dynamic behavior of photogenerated carries is highly important in the photocatalysis for mechanism clarifications (Pattengale et al., 2016), however has never been investigated during the photoreduction of Cr(VI), as the charge separation dynamic process generally occurs on the nanosecond time scale.

Herein, we chose an amino functionalized iron based MOF called NH_2-MIL-88B–Fe (Fe-MOF) as the objective for further modification because of its good stability (Shi et al., 2015). Briefly, the MoS_2 was uniformly distributed into the structure of the Fe-MOF to gain the hybrids (named as MF) by a simple modified organic thermal synthesis method. The ability of the MF to alleviate aqueous Cr(VI) contamination under visible light radiation was investigated systematically. In addition, the stability and repeatability of the MF were evaluated. Finally, the mechanisms behind the enhanced photoreduction performance of Cr (VI) was synthetically investigated. In particular, the real-time charge separation kinetics within the hybrids were tracked through the nanosecond time-resolved transient absorption spectroscopy (TA), which quantified the lifetime of photogenerated carriers and provided insights into the important role of the heterojunction from a microscopic perspective.

2. Experimental

2.1. Chemicals and agents

All of reagents were purchased through commercial means, and used directly without further purification unless specifically mentioned. Molybdenum disulfide (MoS_2), 2-aminoterephthalic acid (NH_2-BDC), diphenylcarbazide, ferric chloride hexahydrate ($FeCl_3{\cdot}6H_2O$), N,N-dimethylformamide (DMF), methanol (MeOH), ethanol (EtOH), acetone, sodium persulfate ($Na_2S_2O_8$), potassium dichromate ($K_2Cr_2O_7$), potassium hydroxide (KOH), sulfuric acid (H_2SO_4), Nafion® 117 solution.

2.2. Preparation of MF

Fe-MOF was synthesized according to a modified one-step solvothermal synthesis method (Li et al., 2018). Typically, $FeCl_3{\cdot}6H_2O$ (3 mM, 0.8109 g) and NH_2-BDC (3 mM, 0.5435 g) were dissolved in 67 mL of DMF solution. This mixture was transferred into the tank of the Teflon-lined autoclave and stirred rapidly for 30 min, followed by a 24 h reaction at 150 °C. Subsequently, the suspension was centrifuged at 10000 rpm for 10 min to obtain a reddish brown product, which was washed three times with ethanol before dried in a 150 °C oven for 12 h.

MF was prepared using the same preparation process as described above, except that DMF solution was replaced with different MoS_2/DMF dispersion solution which was prepared by continuous ultrasonic treatment for 1 h. For a reference, composites with different mass ratios of MoS_2 and Fe-MOFs were marked as MF-0.5 (0.5 %), MF-1.0 (1.0 %), MF-1.5 (1.5 %) and MF-2.0 (2.0 %), respectively.

2.3. Characterizations

Morphological information of photocatalysts before and after MoS_2 modification was investigated by scanning electron microscopy (SEM) with 1.00 kV operating voltage, 20000 to 200000 magnification, and 3.3 mm working distance, and a field-emission transmission electron microscope (FETEM) with an acceleration voltage of 200 kV. The crystalline phase of the photocatalysts was performed on an X-ray diffractometer (XRD) with Cu Kα as radiation source ($\lambda = 0.154056$ nm) (Yuan et al., 2019). The functional groups information for materials was recorded using Fourier transform infrared spectroscopy (FTIR). The element composition of the samples was detected with an X-ray photoelectron spectroscopy (XPS) using monochromatic Al Kα as radiation source. The optical property of the samples was measured using UV–visible–near-infrared spectrophotometer with $BaSO_4$ as the internal reference. Luminescence properties of the composites were explored using a steady-state/transient fluorescence spectrometer at 250 nm excitation. A micromeritics instrument was used to measure the Brunauer-Emmett-Teller (BET) specific surface area (SSA) and pore volume distribution by nitrogen adsorption-desorption at 77 K. The surface charge distribution state of the samples was carried out on a Nanoparticle size and potential analyzer.

All electrochemical characterizations were conducted in the same three-electrode system with FTO glass electrode modified with the photocatalysts, Pt wire and Ag/AgCl electrode, and 0.5 M Na_2SO_4 as the working electrode, counter electrode, reference electrode, and electrolyte solution, respectively. The detailed process of the preparation of the working electrode was presented in supporting information (SI). Electrochemical impedance spectroscopy (EIS) characterization was proceeded on a Multichannel electrochemical workstation with a frequency range from 0.05 Hz to 200 kHz. The Mott-Schottky measurements were implemented on an electrochemical workstation with light shield. Transient photocurrent responses were conducted by an electrochemical workstation under intermittent visible light illumination. Electron spin resonance (ESR) signals for the photocatalysts were recorded on an electron paramagnetic resonance spectrometer under visible light radiation at 298 K (Wang et al., 2011).

The experimental scheme of nanosecond time-resolved TA spectroscopy is described in detail in SI.

2.4. Photocatalytic experiments

Since the photocatalysts have a strong adsorption capacity for Cr(VI) in this process, which hardly reached the adsorption-desorption equilibrium in the actual test, the adsorption and the photoreduction processes were separately discussed according to the previous work (Fang

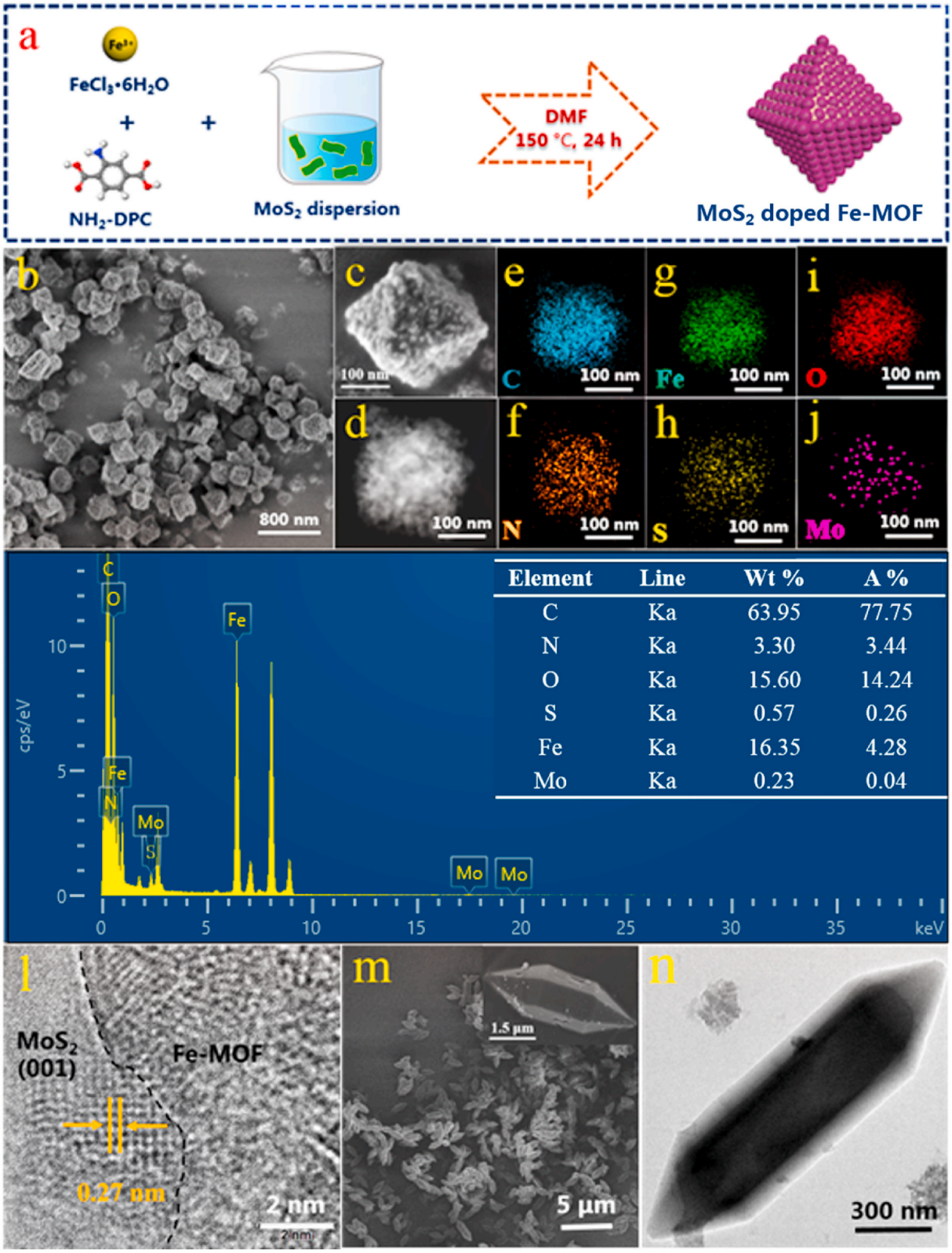

Fig. 1. (a) Process diagram for the preparation of 1.5 wt % molybdenum disulfide doped iron-based metal organic framework; (b), (c) scanning electron microscopy and (d) field-emission transmission electron microscope images of 1.5 wt % molybdenum disulfide doped iron-based metal organic framework; (e–k) energy dispersive spectrometer mapping and spectra, and (l) high resolution transmission electron microscopy images of 1.5 wt % molybdenum disulfide doped iron-based metal organic framework; (m) scanning electron microscopy and (n) transmission electron microscope of iron-based metal organic framework.

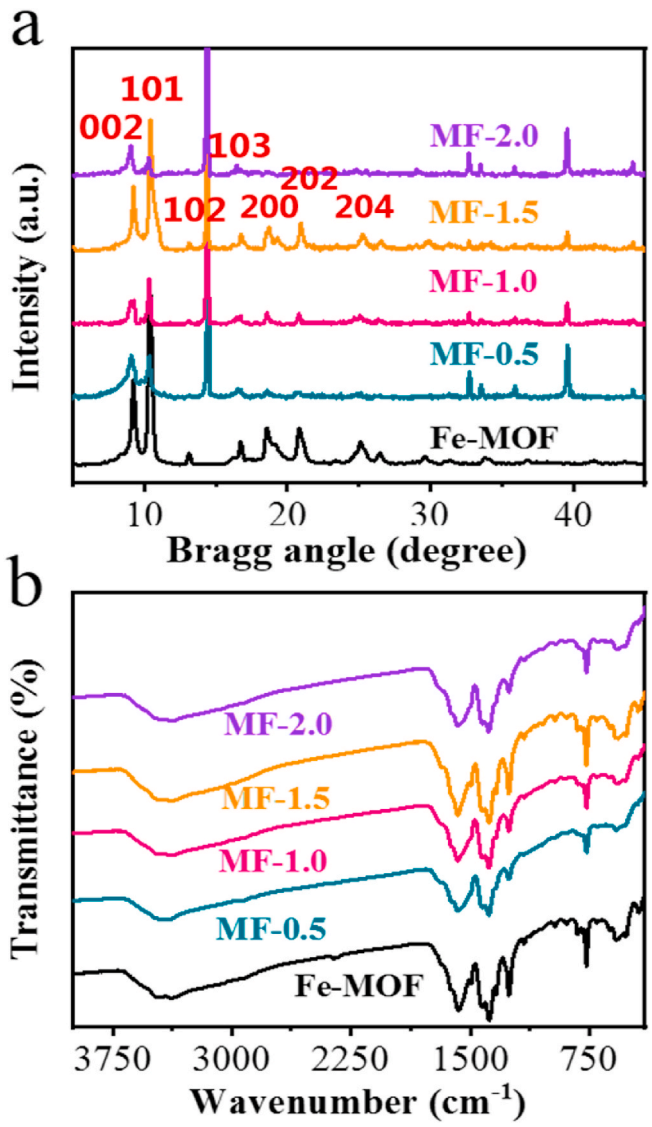

Fig. 2. (a) X-ray diffractometer patterns and (b) Fourier transform infrared spectroscopy spectra of iron-based metal organic framework and molybdenum disulfide doped iron-based metal organic framework.

et al., 2019).

All batches of photoreduction experiments were conducted under visible light radiation by a 300 W xenon lamp system with the 420 nm cutoff filter at room temperature. In detail, 40 mg of the photocatalysts were dispersed in 40 mL of 20 mg L^{-1} Cr(VI) solution with the pH adjusted to 2.0 using 0.1 M H_2SO_4, and 1 mL methanol was added to the system as a sacrificial agent to provide electrons. After rapid stirring, the photoreduction experiments were initiated by illumination of above dispersion. Afterward, 2 mL of the suspension was collected for further centrifugation and filtration to gain the supernatant at a given time interval. The concentration of Cr(VI) in the supernatant was determined by the 1,5-diphenylcarbazide colorimetric method (DPC) (Qiang et al., 2020). The removal efficiency of Cr(VI) was expressed as $C/C_0 \times 100\%$, where C_0 and C represent initial Cr(VI) concentration and the Cr(VI) concentration at a certain time, respectively. The repeatability and stability of the photocatalysts were explored by repeated photoreduction experiments and XRD characterization of the materials after each reaction.

In the adsorption experiments, the test conditions were kept identical with those of photoreduction experiments, except for the entire system was placed under dark conditions.

3. Results and discussion

3.1. Morphology and construction of the photocatalysts

SEM and HRTEM images were recorded to provide detailed morphological information of prepared photocatalysts before and after MoS_2 modification. Figs. S1a and S1b show that the pure MoS_2 exhibited a micron-sized sheet with a uniform surface and thickness, keeping in line with the results of atomic force microscopy (AFM), where the MoS_2 was multi-layer flake with a 60 nm thickness of the single flake (Fig. S2a-c). Moreover, the Fe-MOF appears to be spindle-like with lengths ranging from 3.0 to 4.5 μm and widths ranging from 300 to 500 nm (Figs. 1m and n), which are consistent with previous reports (Wu et al., 2016). Surprisingly, the introduction of MoS_2 changed the shape of the composites from the original spindle to octahedron with a rough surface (Fig. 1b and c). It is speculated that these changes the attachment of MoS_2 to the crystal surface of Fe-MOF prevented its further growth (Cai et al., 2016). In fact, the transition from micron to nanometer of Fe-MOF is beneficial to its full contact with visible light and exposure of more adsorption and reactive sites for contaminants. As expected, there was an obvious boundary (Fig. 1k) on the left with the lattice spacing of 0.27 nm, which belongs to the (100) crystal plane of 2H phase MoS_2 (Li et al., 2014), and the right part was assigned to Fe-MOF. However, no apparent lattice stripes were observed for Fe-MOF since the construction of MOF materials was based on coordination, which was so fragile that it was difficult to retain complete lattice information under the bombardment of high energy electron beams (Liang et al., 2015). Furthermore, the HRTEM image also shows that the fragmented MoS_2 nanosheets were uniformly dispersed in the structure of Fe-MOF with exposed (100) crystal planes (Fig. S1c), similar heterojunction boundaries are also observed in Fig. S1d. These findings suggest that the heterojunction is indeed formed at the phase interface between MoS_2 and Fe-MOF. Besides, the energy dispersive spectrometer (EDS) mapping (Fig. 1e–j) and spectra (Fig. 1k) also illustrate the coexistence of different elements, where all elements were uniformly distributed within the hybrid.

Crystalline phase of the obtained hybrid material was analyzed by XRD. As displayed in Fig. 2a, the diffraction peaks of Fe-MOF can be well assigned to the (002), (101), (102), (103), (200), (202), (302) and (204) planes (Wang et al., 2011). The MF had the same diffraction peaks compared with pristine Fe-MOF, indicating that the retained Fe-MOF structure after MoS_2 modification. Meanwhile, there are some new characteristic peaks (Fig. S3) with bragg angles at 15°, 33° and 40° corresponding to the (002), (100) and (103) crystal planes of 2H–MoS_2, respectively (Hu et al., 2010). Additionally, the reduction of the intensity of partial diffraction peaks for the composites in comparison with pure Fe-MOF and MoS_2, is stemmed from the mutual covering effect of some crystal surfaces between the two components (Zhang and Park, 2019).

The functional groups information for Fe-MOF and MF were studied by FTIR spectroscopy as depicted in Fig. 2b. The same vibration peaks in the photocatalysts before and after MoS_2 modification signified no change in molecular structure of Fe-MOF with MoS_2 modification. In detail, the peak appeared at 570 cm^{-1} indicated the telescopic vibration of Fe–O bond in MOF, while the peaks appeared at 767 cm^{-1} and 1255 cm^{-1} were assigned to the vibration peaks of C–H and C–N bonds on the benzene ring, respectively (Wu et al., 2016). Moreover, a pair of spikes peaks emerged at 1384 cm^{-1} and 1572 cm^{-1} corresponded to the telescopic vibration of carboxyl groups, and the wide peaks observed at 3378 cm^{-1} and 3486 cm^{-1} could be attributed to the asymmetric and symmetrical vibration of amino groups.

The chemical states and elemental compositions of prepared photocatalysts were explored via XPS in Fig. 3a, where the survey scanning spectra of MF-1.5 clearly stated that Fe-MOF and MoS_2 coexist in the composites. The Mo 3d orbital of MoS_2 was deconvoluted into the following primary four peaks: peak of Mo^{4+} $3d_{3/2}$ (232.9 eV) (Peng et al., 2019); peak of Mo^{4+} $3d_{5/2}$ (229.8 and 229.4 eV) (Zhou et al.,

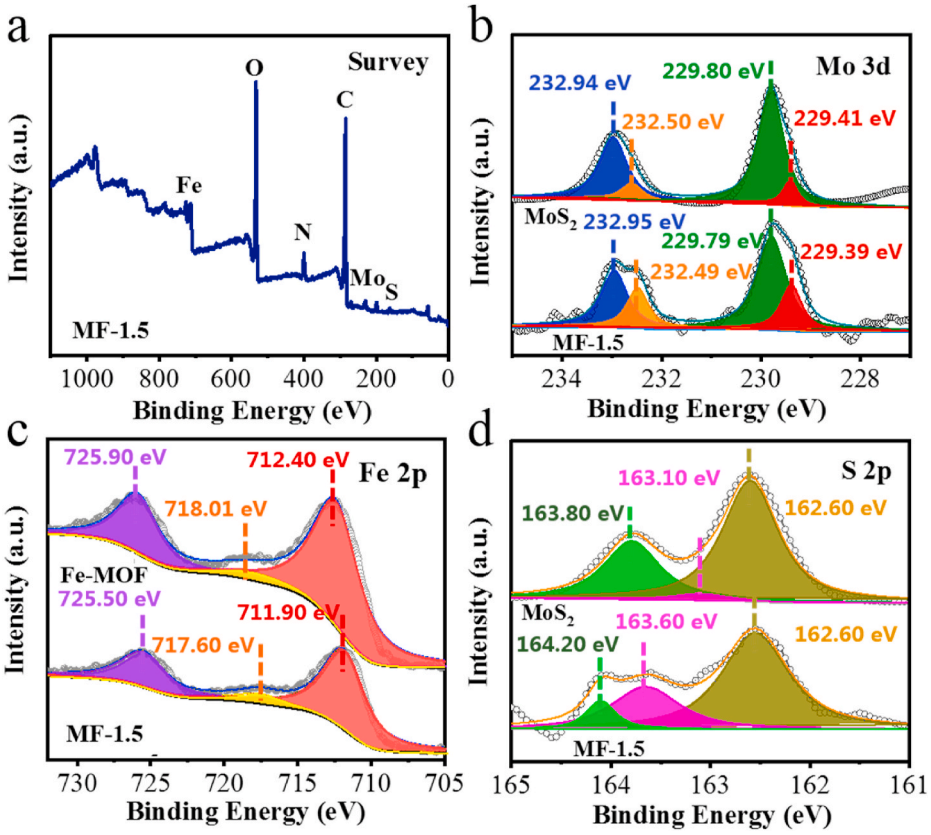

Fig. 3. X-ray photoelectron spectroscopy of as prepared samples: (a) survey spectrum of 1.5 wt % molybdenum disulfide doped iron-based metal organic framework; (b) Mo 3d of molybdenum disulfide and 1.5 wt % molybdenum disulfide doped iron-based metal organic framework; (c) Fe 2p of iron-based metal organic framework and 1.5 wt % molybdenum disulfide doped iron-based metal organic framework; (d) S 2p of molybdenum disulfide and 1.5 wt % molybdenum disulfide doped iron-based metal organic framework.

2013); peak of Mo^{6+} species (232.5 eV) (Liu et al., 2016), of which the Mo^{6+} was the product of partially oxidized MoS_2 (Lonkar et al., 2020). In addition, there was an apparent change of the Mo^{4+}/Mo^{6+} peak area in the hybrid, which might be due to the electron transfer between Mo and Fe through the Mo–O–Fe bond (Xing et al., 2018). Besides, the high-resolution Fe 2p spectrum of Fe-MOF could be divided into three peaks located at 712.4, 718.0 and 725.9 eV (Fig. 3c), corresponding to iron(III) oxide (Shi et al., 2015). Meanwhile, as shown in Fig. 3d, the three peaks centered at 162.6, 163.1 and 163.8 eV in the S 2p spectrum of MoS_2 may be ascribed to S^{2-} $2p_{3/2}$, S_2^{2-} species and S^{2-} $2p_{1/2}$, respectively (Lonkar et al., 2020; Pan et al., 2018; Qiang et al., 2021). Apparently, there was an 0.4 eV deviation at high binding energy corresponding to the transition of S^{2-} to S_2^{2-} species and an 0.4 eV overall shift of Fe 2p peaks toward low binding energy after the MoS_2 doping into Fe-MOF, indicating the electron transfer between Fe and S^{2-} species caused by the formation of heterojunction in the hybrid (Fig. 3c and d). The above results clearly demonstrate the formation of heterojunction between Fe-MOF and MoS_2 in the hybrid, in consistent with the HRTEM results (Wang et al., 2018). Taken together, the hybrids derived from Fe-MOF modified by MoS_2 was successfully prepared.

3.2. Optical property of the photocatalysts

Optical properties of Fe-MOF and MF were examined by UV–visible–near-infrared spectrophotometer. As shown in Fig. 4a, Fe-MOF had best responses to visible light, which was in line with previous reports (Laurier et al., 2013). Unexpectedly, the response of all composites to visible light declined, which probably were attributed to the blocking of visible light adsorption caused by MoS_2. Moreover, the band gap (E_g) of all photocatalysts was calculated according to Tauc plot method as follows (Balu et al., 2020; Li et al., 2020; Wang et al., 2019):

$$(\alpha h\nu)^{1/n} = A(h\nu - E_g) \quad (1)$$

where α, *h*, *ν*, and A represent the absorption index, Planck's constant, frequency, and proportionality constant, respectively. The value of n was defined by the type of semiconductor bandgap and here 1/2 was taken since direct allowed transition (Wang et al., 2020). The final E_g value was determined by extrapolating the straight-line region of $(\alpha h\nu)^2$ vs. hν plot to the horizontal axis (Challagulla et al., 2016; Wang et al., 2016). As shown in Fig. 4b, the E_g values of Fe-MOF, MF-0.5, MF-1.0, MF-1.5 and MF-2.0 were calculated to be 2.48, 2.45, 2.41, 2.37 and 2.42 eV, respectively, demonstrating that the introduction of MoS_2 with an optimum dosage at 1.5 % was beneficial for enhancing the separation process of photogenerated carriers of Fe-MOF.

3.3. Adsorption and photocatalytic evaluation

The photoreduction experiments of Cr(VI) were performed with MF, Fe-MOF and MoS_2 under visible light irradiation. Interestingly, since both Fe-MOF and MF were found to possess good adsorption capacity for aqueous Cr(VI) during experiments, the adsorption-desorption equilibrium could not be reached before the illumination was given (Fig. S4). In general, MF showed a better performance with an adsorption capacity of 98.9 % within 4 h of reaction than Fe-MOF (about 5 h). The results of BET excluded the assumption that the enhancement of adsorption ability originates from the increase of the specific surface area (SSA), because the SSA of MF sharply reduced after modification by MoS_2 (Table S1). Considering the presence of Cr(VI) in the form of dichromate ($Cr_2O_7^{2-}$) in water, it is believed that the amount of adsorption is determined by the amount of positive charge on the surface of the composite (Fang et al., 2019). Zeta potential results (Fig. S5) revealed that MoS_2 modification could tailor charge distribution on the surface of composites, increasing the abundance of positive charges on the surface and the capacity for Cr(VI) adsorption.

As depicted in Fig. 5a, while only 52 % of Cr(VI) was reduced in Fe-MOF systems under visible-light illumination over 60 min, the

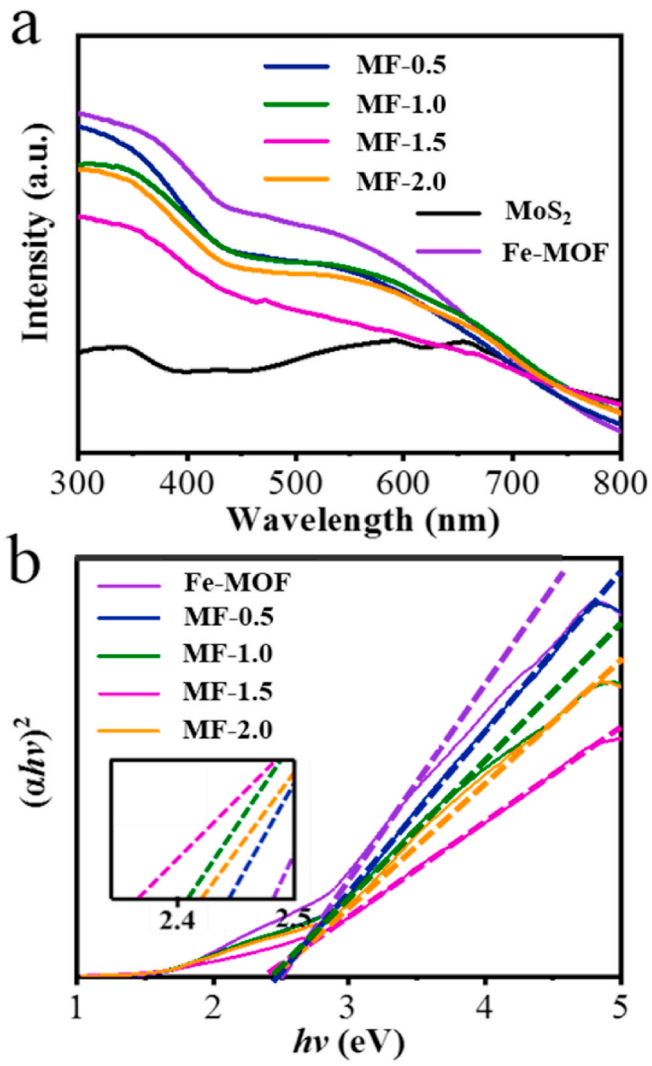

Fig. 4. (a) UV–vis diffuse reflection spectra of molybdenum disulfide, iron-based metal organic framework and molybdenum disulfide doped iron-based metal organic framework; and (b) plot of the $(\alpha hv)^2$ versus hv for iron-based metal organic framework and molybdenum disulfide doped iron-based metal organic framework.

photoreduction efficiency for Cr(VI) substantially improved to 99 % after the modification of MoS_2. The optimal doping dosage of MoS_2 for Cr(VI) photoreduction was observed to be 1.5 %, together with a kinetic rate constant of 0.0553 min^{-1} being 4 times that of the pure Fe-MOF (0.0143 min^{-1}) and 7 times that of MoS_2 (0.0080 min^{-1}) (Fig. 5b). The decrease of the photocatalytic ability of MF-2.0 might be caused by reduced visible light absorption when excessive MoS_2 was introduced. Subsequently, the photocatalysts after a 60-min reaction were collected for further XPS characterization to investigate the oxidation state of Cr species on photocatalysts surface. As shown in Fig. 5c, the two peaks located at 587.2 and 577.4 eV corresponding to Cr(III) but no characteristic peaks of Cr(VI) proved the complete photoreduction of adsorbed Cr(VI) (Zhao et al., 2017). That is, the introduction of MoS_2 significantly improved the photocatalytic performance of Fe-MOF. Notably, the Cr (VI) photoreduction rates of various catalysts are listed in Table 1 to make a comparison between the hybrid material in our work and those reported. Evidently, 1.5 wt % MoS_2 doped Fe-MOF had the highest photoreduction rate compared with all reported MOF-based photocatalysts, which took less time to achieve 100 % Cr(VI) photoreduction efficiency than most of MOF-based photocatalysts except for NH_2-MIL-88(Fe) and TiO_2@NH_2-MIL-88B(Fe), indicating that the capability of hybrid photocatalyst in the study may need an improvement especially for the treatment of low concentration Cr(VI). In particular, precisely because the limitation of intrinsic defects, the iron-based MOF modified by metal oxides had dependence on ultraviolet light after the successful construction of heterojunction. By comparison, our study demonstrates that the iron-based MOF modified with MoS_2 not only improved charge separation efficiency by virtue of the formed heterojunction (Fig. 6a and b), but also regulated the positive charge distribution on the surface of iron-based MOF (Fig. S5) and weakened charge transfer resistance (Fig. S7). Moreover, the dynamic behavior of photogenerated carriers was unclear for Cr(VI) reduction in those previous reports, while for the first time was explored through the nanosecond time-resolved TA spectroscopy in our study, as will be discussed later. Additionally, a comparable photoreduction rate was obtained when compared with traditional inorganic semiconductor photocatalysts, as listed in Table 1. On the other hand, the results of conditional experiments also showed that the photoreduction efficiency of Cr(VI) was positively correlated with the concentration of photocatalysts (Fig. 5d).

Generally, the repeatability and stability of the photocatalysts also play important roles in their practical application. Specifically, the MF-1.5 was successively collected after each reaction followed by cleaning and drying operations for further repeated photoreduction of Cr(VI). The SEM results showed that the morphology of MF-1.5 did not change significantly after the first (Figs. S6c and S6d) and fourth cycle experiments (Figs. S6e and S6f) compared to the fresh one (Figs. S6a and S6b). Moreover, the stability of MF-1.5 crystal structure after the first and fourth cycle experiments were explored by XRD (Fig. 5f). Compared to the fresh one, the diffraction peak intensity of MF-1.5 did not change obviously after the first cycle experiment, and only slightly decrease of the diffraction peak intensities was found after the fourth cycle, which state the hybrids keep excellent tolerance under acidic reaction conditions (Shi et al., 2015; Sun et al., 2014). Besides, the photoreduction efficiency of Cr(VI) was only reduced by 7% after four cycles as depicted in Fig. 5e, indicating MF-1.5 has the practical application potential with a good stability.

3.4. Possible mechanisms of MF boosting Cr(VI) photoreduction

The contribution of heterojunction and improved electrical conductivity were expected to afford encouraging performance of MF in Cr (VI) photoreduction according to the original intention of materials design. EIS results (Fig. S7a) confirm the obvious reduction of the charge transfer resistance (R_{ct}) of Fe-MOF after the introduction of 1.5 % MoS_2, which exhibited the smaller R_{ct} about 743 Ω based on the circuit fitting result (inset in Fig. S7a). It is speculated that uniform interpenetration of MoS_2 within Fe-MOF led to the formation of some electronic channels (Radisavljevic et al., 2011), which should be responsible for enhanced charge transfer. Correspondingly, as shown in Fig. S7b, the charge transfer resistance values of the photocatalysts followed the order: MoS_2 < 1.5 % < 2.0 % < 1.0 % < 0.5 % < Fe-MOF, agreeing well with the order of Cr(VI) reduction efficiency.

The characterization results of HRTEM (Fig. 1f and S1) provided a direct evidence of the formation of heterostructures at the interface between MoS_2 and Fe-MOF. The separation and recombination efficiency of photogenerated carriers within MF has been carefully studied in order to further consolidate our hypothesis. In general, the recombination efficiency of photocarriers is greatly suppressed due to the formation of heterostructures (Li et al., 2019; Xiang et al., 2012). Accordingly, the variations of the photogenerated carrier recombination efficiency of the MF were characterized through the photoluminescence (PL) spectrum. In general, the increase of PL intensity indicate the recombination aggravation (Ma et al., 2019; Shoueir et al., 2019). As displayed in Fig. 6a, almost no significant fluorescence peak was observed for MF-1.5 compared to MoS_2 and Fe-MOF, proving that the doping of MoS_2 was favorable for repressing photogenerated

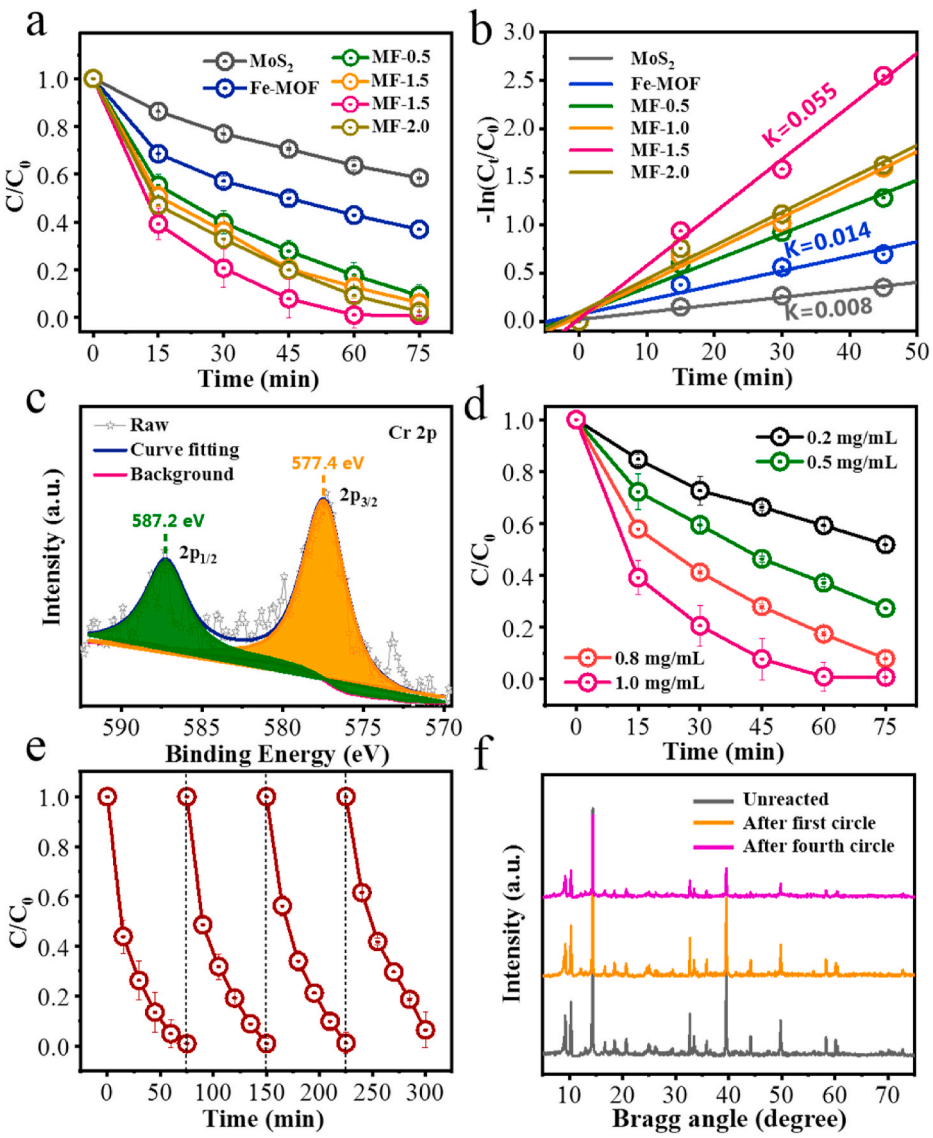

Fig. 5. (a) Photocatalytic reduction of Cr(VI) experiments and (b) first-order kinetic fitting over molybdenum disulfide, iron-based metal organic framework and molybdenum disulfide doped iron-based metal organic framework; (c) Cr 2p spectrum of 1.5 wt % molybdenum disulfide doped iron-based metal organic framework after reaction; (d) Effect of 1.5 wt % molybdenum disulfide doped iron-based metal organic framework concentration on the photoreduction of Cr(VI); (e) Repeatability test and (f) stability characterization of 1.5 wt % molybdenum disulfide doped iron-based metal organic framework.

Table 1
Comparison of photoreduction of Cr(VI) with various photocatalysts.

Photocatalysts	Reaction conditions (photocatalyst dosage, pH, initial Cr(VI) concentration, light source)	Photoreduction efficiency	Photoreduction rate	Reference
UiO-66-NH_2(Zr/Hf)	0.16 mg L^{-1}, 2.0, 5 mg L^{-1}, Visible	120 min, 100 %	2.5 mg L^{-1} h^{-1}	Du et al. (2019)
NNU-36/15	0.375 mg L^{-1}, 2.17, 8 mg L^{-1}, Visible	60 min, 95 %	7.6 mg L^{-1} h^{-1}	Zhao et al. (2017)
MIL-53(Fe)/SnS	1 mg L^{-1}, 2.0, 20 mg L^{-1}, Sunlight	60 min, 70 %	3.5 mg L^{-1} h^{-1}	Xia et al. (2018)
WO_3/MIL-53(Fe)	2.0 mg L^{-1}, 2.5, 10 mg L^{-1}, Sunlight	450 min, 80 %	0.8 mg L^{-1} h^{-1}	Oladipo et al., 2018
WO_3@MIL-100(Fe)	0.25 mg L^{-1}, 2.0, 5 mg L^{-1}, Visible	120 min, 100 %	2.5 mg L^{-1} h^{-1}	Wang et al. (2020)
NH_2-MIL-88B (Fe)	0.5 mg L^{-1}, 2.0, 8 mg L^{-1}, Visible	45 min, 100 %	10.7 mg L^{-1} h^{-1}	Shi et al. (2015)
TiO_2@NH_2-MIL-88B(Fe)	0.5 mg L^{-1}, 4.0, 20 mg L^{-1}, Sunlight	40 min, 100 %	15 mg L^{-1} h^{-1}	Yuan et al. (2019)
1.5 wt % MoS_2 doped MOF	1.0 mg L^{-1}, 2.0, 20 mg L^{-1}, Visible	65 min, 100 %	19.8 mg L^{-1} h^{-1}	This work
$Bi_{12}GeO_{20}$/g-C_3N_4	3 mg L^{-1}, 2.5, 10 mg L^{-1}, Visible	180 min, 100 %	3.3 mg L^{-1} h^{-1}	Wan et al. (2017)
Bi_2MoO_6/ZnO	2 mg L^{-1}, 2.0, 50 mg L^{-1}, Visible	150 min, 100 %	20.0 mg L^{-1} h^{-1}	Zhang et al. (2019)
Carbon dots-TiO_2 nanosheets	1 mg L^{-1}, 2.0, 10 mg L^{-1}, Sunlight	120 min, 99 %	5.0 mg L^{-1} h^{-1}	Li et al., 2018

electron-hole recombination. Subsequently, the influence of MoS_2 modification for photogenerated electron-hole separation was further investigated using transient photocurrent response curve, where the separation efficiency of photogenerated carriers was determined by the magnitude of the photogenerated current (Feng et al., 2020). As indicated in Fig. 6b, the photocurrent intensity of photocatalysts obeyed the order of MF-1.5>Fe-MOF>MoS_2, which revealed that MoS_2 doping clearly boosted the separation efficiency of photogenerated carriers. The gradual decrease of photocurrent may be due to the fact that the electrode surface is not completely stable during the test.

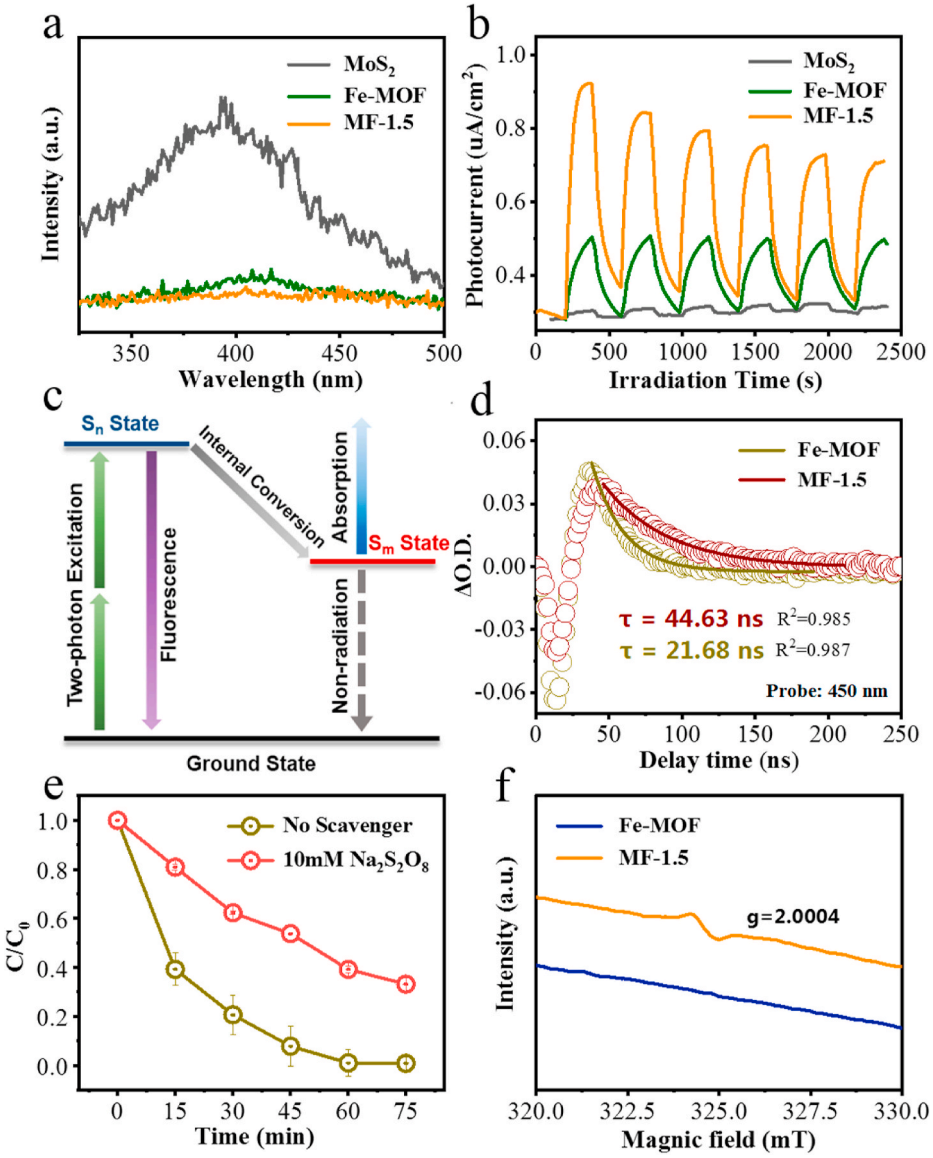

Fig. 6. (a) Photoluminescence spectra and (b) transient photocurrent response curve for molybdenum disulfide, iron-based metal organic framework and 1.5 wt % molybdenum disulfide doped iron-based metal organic framework; (c) The charge separation schematic diagram of 1.5 wt % molybdenum disulfide doped iron-based metal organic framework, and (d) the nanosecond transient absorption kinetics at 450 nm of the photocatalysts for excitation under 532 nm laser. (e) Photoelectrons trapping experiment of 1.5 wt % molybdenum disulfide doped iron-based metal organic framework; (f) Electron spin resonance spectra of iron-based metal organic framework and 1.5 wt % molybdenum disulfide doped iron-based metal organic framework under the radiation of visible light.

Particularly, considering the nature of photocatalytic processes, that is, the charge separation steps take place in nanosecond scale, nanosecond time-resolved TA spectroscopy were used to explore the real-time charge separation dynamics (Grigioni et al., 2018) in the materials before and after the formation of interfacial heterojunction. As shown in Fig. 6c, the photocatalysts were excited to Sn state by two-photon excitation of 532 nm laser, which is evidenced by the similarity between the steady-state fluorescence emission spectra under 280 nm (Fig. 6a) and the transient fluorescence emission spectra under 532 nm (Fig. S8). After excited to Sn state for MF-1.5, Sm state with lower energy levels and better stability were formed through internal conversion (IC) (Wei et al., 2017) induced by heterojunction compare to the fast luminous process inside Fe-MOF. Moreover, the lifetime of Sn and Sm state could be characterized by investigating the TA kinetic process. As kinetic profiles detected within the range of 350–500 nm show no discernible difference, a typical set of data at 450 nm was selected to represent the kinetic processes of photocatalysts (Fig. 6d). Compared with the lifetime of Sn state about 21.68 ns in Fe-MOF, the lifetime of Sm state notably increased to 44.63 ns in MF-1.5, which is conducive to the occurrence of subsequent reduction process of Cr(VI). As a results, the doping of MoS_2 fundamentally improved the utilization of photogenerated electrons.

On the other hand, the removal rate of Cr(VI) decreased by 74.3 % following the addition of photogenerated electrons scavenger ($Na_2S_2O_8$) into the system (Fig. 6e), highly suggesting the important role of photogenerated electrons in Cr(VI) removal. In addition, the ESR results in the Fig. 6f demonstrated that MF-1.5 exhibited a significant signal peak with a g value of 2.0004 belong to the characteristic peak of the electron in the visible light radiation (Shi et al., 2015), where Fe-MOF did not show any typical ESR signal in the same case. Besides, the Mott-Schottky measurement illustrated the band structure and intrinsic electronic properties of MoS_2, Fe-MOF and MF-1.5 from a thermodynamic point of view. As depicted in Fig. 7a, the positive slope of linear fitting indicated that MF-1.5 was a n-type semiconductor (Yuan et al., 2019). As a consequence, the flat band potential (E_{FB}) of MF-1.5 was determined to be −0.17 eV (pH = 6.8) vs. Ag/AgCl electrode using the extrapolation to $1/C^2 = 0$. It was also equal to 0.43 eV vs. NHE (pH = 6.8) according to eq. (2) (Sun et al., 2019; Wang et al., 2019).

$$E_{FB\ (vs.\ NHE)} = E_{FB\ (pH\ =\ 0,\ vs.\ Ag/AgCl)} + E_{AgCl} + 0.059*pH \quad (2)$$

where the value of E_{AgCl} is 0.197 eV and the pH value of the system is ca. 6.8 (Liu et al., 2020). Usually, there is an approximate process that the conduction band potential (E_{CB}) of n-type semiconductors is generally

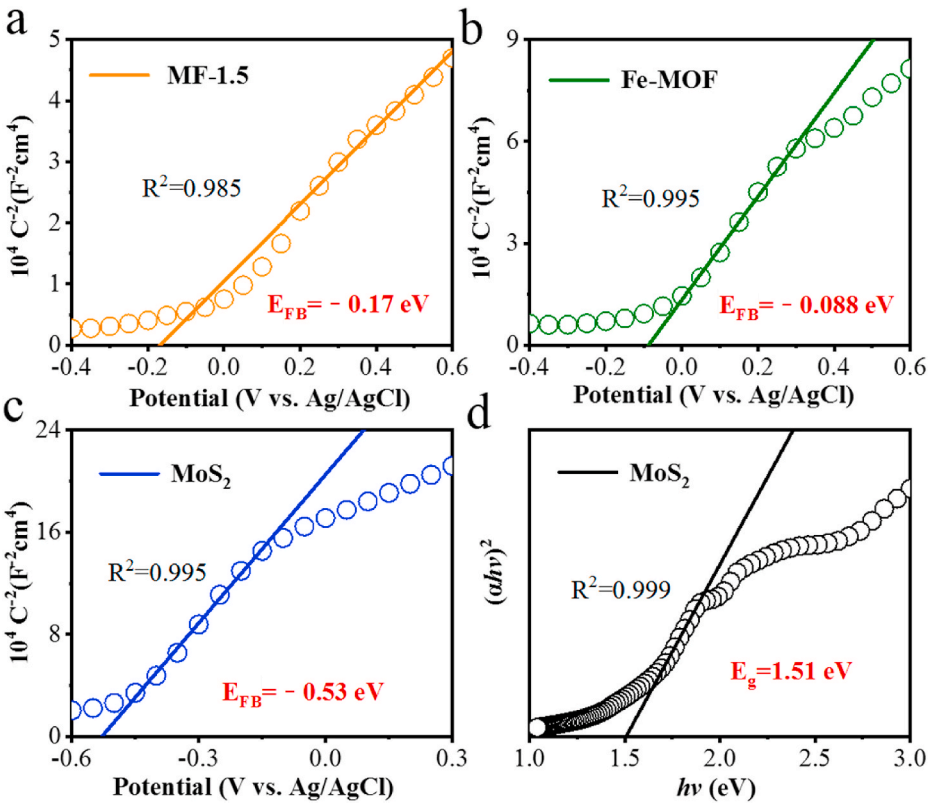

Fig. 7. (a), (b) and (c) typical Mott-Schottky plots of 1.5 wt % molybdenum disulfide doped iron-based metal organic framework, iron-based metal organic framework and molybdenum disulfide; (d) plot of the $(\alpha hv)^2$ versus hv for molybdenum disulfide.

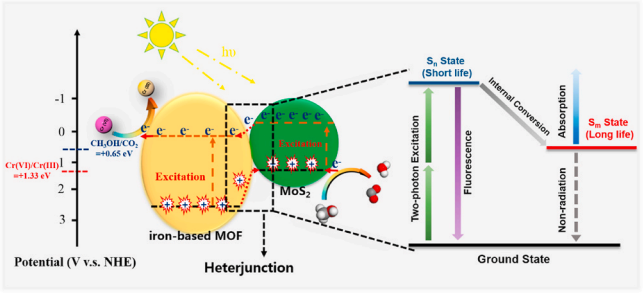

Fig. 8. Proposed mechanism of hexavalent chromium photoreduction by molybdenum disulfide doped iron-based metal organic framework under visible light radiation. The red, gray and white spheres represent oxygen, carbon and hydrogen atoms, respectively. (For interpretation of the references to color in this figure legend, the reader is referred to the Web version of this article.)

lower than that of E_{FB} about 0.3 eV (Xu et al., 2015), so the E_{CB} of MF-1.5 is located at 0.13 eV, which is more negative than the Cr^{6+}/Cr^{3+} couple potential (1.33 V vs. NHE) (Saha et al., 2011), suggesting that the photoelectrons on the conduction band of MF-1.5 had sufficient reduction ability to realize Cr(VI) to Cr(III) in thermodynamics. Similarly, the E_{CB} and valence bands (E_{VB}) of Fe-MOF (Fig. 7b) and MoS_2 (Fig. 7c and d) are at 0.21, 2.69 eV vs. NHE, and −0.23, 1.28 eV vs. NHE, respectively. Although the electrons on the conduction bands of MoS_2 and Fe-MOF also have the ability to reduce Cr(VI), the excited photogenerated electrons will quickly recombine due to the lack of heterojunction, thus showing the limited photoreduction ability of Cr(VI) in the actual process.

In conclusion, the whole process of electron transfer is shown in the following mechanism diagram (Fig. 8). Under visible light excitation, the electrons excited to the MoS_2 conduction band will quickly migrate to the Fe-MOF conduction band under the effect of the IC caused by the heterojunction, and then be utilized by the Cr(VI) adsorbed on its surface. Meanwhile, the holes trapped in the Fe-MOF valence band will also move to the MoS_2 valence band to complete the continuous supply of electrons depending on sacrificial methanol. Overall, the pathway of Cr (VI) photoreduction by MF-1.5 under visible light radiation was proposed as follows:

$$MF - 1.5 + h\nu \rightarrow h^+ + e^- \quad (3)$$

$$Cr_2O_7^{2-} + 6e^- + 14H^+ \rightarrow 2Cr^{3+} + 7H_2O \quad (4)$$

$$CH_3OH + h^+ \rightarrow H_2O + CO_2 \quad (5)$$

4. Conclusions

The unique photocatalyst was successfully obtained through the introduction of molybdenum disulfide in the process of iron-based metal organic framework synthesis in this paper. The regulation of the positive charge on the iron-based metal organic framework surface by molybdenum disulfide realizes the rapid adsorption of hexavalent chromium, which provides a premise for the further efficient photoreduction process. Deeply, the introduction of molybdenum disulfide greatly facilitated the separation efficiency of photoproduced carriers and extended the life of photoproduced electrons owing to the effect of heterogeneous junction formed between the interface of molybdenum disulfide and iron-based metal organic framework. Moreover, rapid migration of photoproduced electrons within the composite materials was also realized with the help of the excellent electron conduction capability of molybdenum disulfide. These superior performances comprehensively resulted in excellent capacity toward hexavalent chromium reduction of molybdenum disulfide doped iron-based metal organic framework under visible light radiation. Finally, the photogenerated electrons have been confirmed as the most important active species by free radical

trapping experiments in the whole photoreduction process. Overall, this work affords a deep insight into role of the heterojunction from a microscopic perspective, which provides inspiration for the preparation of highly-efficient environmental functional photocatalysts based on iron-based metal organic frameworks.

CRediT authorship contribution statement

Wen-Qiang Li: Methodology, Data curation, Writing – original draft, preparation. **Yi-Xuan Wang:** Investigation, Data curation, Writing – original draft. **Yuan-Ming Li:** Methodology, Data curation. **Chuan-Shu He:** Writing – review & editing, Supervision. **Bo Lai:** Investigation, Writing – review & editing. **Fei Chen:** Methodology, Writing – review & editing. **Hui-Juan Wang:** Data curation. **Xiao-Guo Zhou:** Visualization. **Yang Mu:** Data curation, Writing – review & editing, Supervision.

Declaration of competing interest

The authors declare that they have no known competing financial interests or personal relationships that could have appeared to influence the work reported in this paper.

Acknowledgements

The authors appreciate the financial support provided by the National Natural Science Foundation of China (52025101, U19A20108, 51908530 and 51878637).

Appendix A. Supplementary data

Supplementary data to this article can be found online at https://doi.org/10.1016/j.jclepro.2021.128513.

References

Balu, S., Chen, Y.L., Juang, R.C., Yang, T.C., Juan, J.C., 2020. Morphology-controlled synthesis of alpha-Fe_2O_3 nanocrystals impregnated on g-C_3N_4-SO_3H with ultrafast Charge separation for photoreduction of Cr(VI) under visible light. Environ. Pollut. 267, 115491.

Borthakur, P., Das, M.R., Szunerits, S., Boukherroub, R., 2019. CuS decorated functionalized reduced graphene oxide: a dual responsive nanozyme for selective detection and photoreduction of Cr(VI) in an aqueous medium. ACS Sustain. Chem. Eng. 7, 16131–16143.

Cai, X., Lin, J., Pang, M., 2016. Facile synthesis of highly uniform Fe-MIL-88B particles. Cryst. Growth Des. 16, 3565–3568.

Challagulla, S., Nagarjuna, R., Ganesan, R., Roy, S., 2016. Acrylate-based polymerizable sol-gel synthesis of magnetically recoverable TiO_2 supported Fe_3O_4 for Cr(VI) photoreduction in aerobic atmosphere. ACS Sustain. Chem. Eng. 4, 974–982.

De Bittencourt, M.A., Novack, A.M., Scherer Filho, J.A., Mazur, L.P., Marinho, B.A., da Silva, A., de Souza, A.A.U., De Souza, S.M., 2020. Application of $FeCl_3$ and TiO_2-coated algae as innovative biophotocatalysts for Cr(VI) removal from aqueous solution: a process intensification strategy. J. Clean. Prod. 268, 122164.

Du, X.D., Yi, X.H., Wang, P., Zheng, W., Deng, J., Wang, C.C., 2019. Robust photocatalytic reduction of Cr(VI) on UiO-66-NH_2(Zr/Hf) metal-organic framework membrane under sunlight irradiation. Chem. Eur J. 356, 393–399.

Fang, Z., Li, Q., Su, L., Chen, J., Chou, K.C., Hou, X., 2019. Efficient synergy of photocatalysis and adsorption of hexavalent chromium and rhodamine B over Al_4SiC_4/rGO hybrid photocatalyst under visible-light irradiation. Appl. Catal. B Environ. 241, 548–560.

Feng, S., Chen, T., Liu, Z., Shi, J., Yue, X., Li, Y., 2020. Z-scheme CdS/CQDs/g-C_3N_4 composites with visible-near-infrared light response for efficient photocatalytic organic pollutant degradation. Sci. Total Environ. 704, 135404.

Grigioni, I., Abdellah, M., Corti, A., Dozzi, M.V., Hammarström, L., Selli, E., 2018. Photoinduced charge-transfer dynamics in WO_3/$BiVO_4$ photoanodes probed through midinfrared transient absorption spectroscopy. J. Am. Chem. Soc. 140, 14042–14045.

Hao, X.Q., Jin, Z.L., Yang, H., Lu, G.X., Bi, Y.P., 2017. Peculiar synergetic effect of MoS_2 quantum dots and graphene on metal-organic frameworks for photocatalytic hydrogen evolution. Appl. Catal. B Environ. 210, 45–56.

Hu, K.H., Hu, X.G., Sun, X.J., 2010. Morphological effect of MoS_2 nanoparticles on catalytic oxidation and vacuum lubrication. Appl. Surf. Sci. 256, 2517–2523.

Laurier, K.G., Vermoortele, F., Ameloot, R., De Vos, D.E., Hofkens, J., Roeffaers, M.B., 2013. Iron(III)-based metal-organic frameworks as visible light photocatalysts. J. Am. Chem. Soc. 135, 14488–14491.

Li, B., Lai, C., Xu, P., Zeng, G., Huang, D., Qin, L., Yi, H., Cheng, M., Wang, L., Huang, F., Liu, S., Zhang, M., 2019. Facile synthesis of bismuth oxyhalogen-based Z-scheme photocatalyst for visible-light-driven pollutant removal: kinetics, degradation pathways and mechanism. J. Clean. Prod. 225, 898–912.

Li, Y., Jiang, J., Fang, Y., Cao, Z., Chen, D., Li, N., Xu, Q., Lu, J., 2018a. TiO_2 nanoparticles anchored onto the metal-organic framework NH_2-MIL-88B(Fe) as an adsorptive photocatalyst with enhanced fenton-like degradation of organic pollutants under visible light irradiation. ACS Sustain. Chem. Eng. 6, 16186–16197.

Li, Y., Li, A., Li, F., Liu, D., Chai, Y., Liu, C., 2014. Application of HF etching in a HRTEM study of supported MoS_2 catalysts. J. Catal. 317, 240–252.

Li, Y., Liu, Z., Wu, Y., Chen, J., Zhao, J., Jin, F., Na, P., 2018b. Carbon dots-TiO_2 nanosheets composites for photoreduction of Cr(VI) under sunlight illumination: favorable role of carbon dots. Appl. Catal. B Environ. 224, 508–517.

Li, Y.X., Fu, H., Wang, P., Zhao, C., Liu, W., Wang, C.C., 2020. Porous tube-like ZnS derived from rod-like ZIF-L for photocatalytic Cr(VI) reduction and organic pollutants degradation. Environ. Pollut. 256, 113417.

Liang, R., Shen, L., Jing, F., Qin, N., Wu, L., 2015. Preparation of MIL-53(Fe)-reduced graphene oxide nanocomposites by a simple self-assembly strategy for increasing interfacial contact: efficient visible-light photocatalysts. ACS Appl. Mater. Interfaces 7, 9507–9515.

Liu, H., Cheng, D.g., Chen, F., Zhan, X., 2020. 2D porous N-deficient g-C_3N_4 nanosheet decorated with CdS Nanoparticles for enhanced visible-light-driven photocatalysis. ACS Sustain. Chem. Eng. 8, 16897–16904.

Liu, H., Hu, H., Wang, J., Niehoff, P., He, X., Paillard, E., Eder, D., Winter, M., Li, J., 2016. Hierarchical ternary MoO_2/MoS_2/heteroatom-doped carbon hybrid materials for high-performance lithium-ion storage. ChemElectroChem 3, 922–932.

Lonkar, S.P., Pillai, V.V., Alhassan, S.M., 2020. Scalable solid-state synthesis of MoS_2-NiS_2/graphene nanohybrids as bifunctional electrocatalysts for enhanced overall water splitting. Mater. Adv. 1, 794–803.

Ma, W., Wang, M., Chen, Z., Meng, F., Cheng, Z., Tan, D., Pan, Y., Duan, S., Gao, J., 2019. Characteristics of novel extraction and photoinduced precipitation approach by PEG/SA and fluorescence monitoring of Cr(VI). ACS Sustain. Chem. Eng. 7, 6323–6334.

Nguyen, T.N., Kampouri, S., Valizadeh, B., Luo, W., Ongari, D., Planes, O.M., Züttel, A., Smit, B., Stylianou, K.C., 2018. Photocatalytic hydrogen generation from a visible-light-responsive metal-organic framework system: stability versus activity of molybdenum sulfide cocatalysts. ACS Appl. Mater. Interfaces 10, 30035–30039.

Pattengale, B., Yang, S.H., Ludwig, J., Huang, Z.Q., Zhang, X.Y., Huang, J., 2016. Exceptionally long-lived charge separated state in zeolitic imidazolate framework: implication for photocatalytic applications. J. Am. Chem. Soc. 138, 8072–8075.

Peng, J., Liu, Y., Luo, X., Wu, J., Lin, Y., Guo, Y., Zhao, J., Wu, X., Wu, C., Xie, Y., 2019. High phase purity of large-sized 1T'-MoS_2 monolayers with 2D superconductivity. Adv. Mater. 31, 1900568.

Qiang, T., Chen, L., Xia, Y., Qin, X., 2020. Dual modified MoS_2/SnS_2 photocatalyst with Z-scheme heterojunction and vacancies defects to achieve a superior performance in Cr(VI) reduction and dyes degradation. J. Clean. Prod. 291, 125213.

Radisavljevic, B., Whitwick, M.B., Kis, A.J.A.N., 2011. Integrated circuits and logic operations based on single-layer MoS_2. ACS Nano 5, 9934–9938.

Saha, R., Nandi, R., Saha, B., 2011. Sources and toxicity of hexavalent chromium. J. Coord. Chem. 64, 1782–1806.

Sheberla, D., Bachman, J.C., Elias, J.S., Sun, C.J., Shaohorn, Y., Dinca, M., 2017. Conductive MOF electrodes for stable supercapacitors with high areal capacitance. Nat. Mater. 16, 220–224.

Shi, L., Wang, T., Zhang, H., Chang, K., Meng, X., Liu, H., Ye, J., 2015. An amine-functionalized iron(III) metal-organic framework as efficient visible-light photocatalyst for Cr(VI) reduction. Adv. Sci. 2, 1500006.

Shoueir, K., Kandil, S., El-hosainy, H., El-Kemary, M., 2019. Tailoring the surface reactivity of plasmonic Au@TiO_2 photocatalyst bio-based chitosan fiber towards cleaner of harmful water pollutants under visible-light irradiation. J. Clean. Prod. 230, 383–393.

Subudhi, S., Swain, G., Tripathy, S.P., Parida, K., 2020. UiO-66-NH_2 metal-organic frameworks with embedded MoS_2 nanoflakes for visible-light-mediated H_2 and O_2 Evolution. Inorg. Chem. 59, 9824–9837.

Sun, Q., Hu, X., Zheng, S., Zhang, J., Sheng, J., 2019. Effect of calcination on structure and photocatalytic property of N-TiO_2/g-C_3N_4@diatomite hybrid photocatalyst for improving reduction of Cr(VI). Environ. Pollut. 245, 53–62.

Trickett, C.A., Osbornpopp, T.M., Su, J., Yan, C., Weisberg, J., Huq, A., Urban, P., Jiang, J., Kalmutzki, M.J., Liu, Q., Baek, J., Headgordon, M.P., Somorjai, G.A., Reimer, J.A., Yaghi, O.M., 2019. Identification of the strong Bronsted acid site in a metal-organic framework solid acid catalyst. Nat. Chem. 11, 170–176.

Wan, Z., Zhang, G., Wu, X., Yin, S., 2017. Novel visible-light-driven Z-scheme $Bi_{12}GeO_{20}$/g-C_3N_4 photocatalyst: oxygen-induced pathway of organic pollutants degradation and proton assisted electron transfer mechanism of Cr(VI) reduction. Appl. Catal. B Environ. 207, 17–26.

Wang, H., Sun, Y., Jiang, G., Zhang, Y., Huang, H., Wu, Z., Lee, S.C., Dong, F., 2018. Unraveling the mechanisms of visible light photocatalytic NO purification on earth-abundant insulator-based core-shell heterojunctions. Environ. Sci. Technol. 52, 1479–1487.

Wang, J.W., Qiu, F.G., Wang, P., Ge, C., Wang, C.C., 2021. Boosted bisphenol A and Cr (VI) cleanup over Z-scheme WO_3/MIL-100(Fe) composites under visible light. J. Clean. Prod. 279, 123408.

Wang, M., Qin, Z., Diao, Z., Li, R., Zhong, J., Ma, D., Chen, Y., 2020. Red phosphorus/carbon nitride van der waals heterostructure for photocatalytic pure water splitting under wide-spectrum light irradiation. ACS Sustain. Chem. Eng. 8, 13459–13466.

Wang, X., Hong, M., Zhang, F., Zhuang, Z., Yu, Y., 2016. Recyclable nanoscale zero valent iron doped g-C_3N_4/MoS_2 for efficient photocatalysis of RhB and Cr(VI) driven by visible light. ACS Sustain. Chem. Eng. 4, 4055–4063.

Wang, X., Liu, W., Fu, H., Yi, X.H., Wang, P., Zhao, C., Wang, C.C., Zheng, W., 2019. Simultaneous Cr(VI) reduction and Cr(III) removal of bifunctional MOF/Titanate nanotube composites. Environ. Pollut. 249, 502–511.

Wang, Z., Ma, W., Chen, C., Ji, H., Zhao, J., 2011. Probing paramagnetic species in titania-based heterogeneous photocatalysis by electron spin resonance (ESR) spectroscopy-A mini review. Chem. Eur J. 170, 353–362.

Wei, Y., Zhou, M., Zhou, Q., Zhou, X., Liu, S., Zhang, S., Zhang, B., 2017. Triplet-triplet annihilation upconversion kinetics of C60-Bodipy dyads as organic triplet photosensitizers. Phys. Chem. Chem. Phys. 19, 22049–22060.

Wu, Z., Chen, C., Wan, H., Wang, L., Li, Z., Li, B., Guo, Q., Guan, G., 2016. Fabrication of magnetic NH_2-MIL-88B (Fe) confined brønsted ionic liquid as an efficient catalyst in biodiesel synthesis. Energy Fuels 30, 10739–10746.

Xia, Q., Huang, B., Yuan, X., Wang, H., Wu, Z., Jiang, L., Xiong, T., Zhang, J., Zeng, G., Wang, H., 2018. Modified stannous sulfide nanoparticles with metal-organic framework: toward efficient and enhanced photocatalytic reduction of chromium (VI) under visible light. J. Colloid Interface Sci. 530, 481–492.

Xiang, Q., Yu, J., Jaroniec, M., 2012. Synergetic effect of MoS_2 and graphene as cocatalysts for enhanced photocatalytic H_2 production activity of TiO_2 nanoparticles. J. Am. Chem. Soc. 134, 6575–6578.

Xing, M.Y., Xu, W.J., Dong, C.C., Bai, Y.C., Zeng, J.B., Zhou, Y., Zhang, J.L., Yin, Y.D., 2018. Metal sulfides as excellent co-catalysts for H_2O_2 decomposition in advanced oxidation processes. Inside Chem. 4, 1359–1372.

Xu, D., Cheng, B., Cao, S., Yu, J., 2015. Enhanced photocatalytic activity and stability of Z-scheme Ag_2CrO_4-GO composite photocatalysts for organic pollutant degradation. Appl. Catal. B Environ. 164, 380–388.

Yuan, R., Yue, C., Qiu, J., Liu, F., Li, A., 2019. Highly efficient sunlight-driven reduction of Cr(VI) by TiO_2@NH_2-MIL-88B(Fe) heterostructures under neutral conditions. Appl. Catal. B Environ. 251, 229–239.

Zhang, G., Chen, D., Li, N., Xu, Q., Li, H., He, J., Lu, J., 2019. Fabrication of Bi_2MoO_6/ZnO hierarchical heterostructures with enhanced visible-light photocatalytic activity. Appl. Catal. B Environ. 250, 313–324.

Zhang, Y., Park, S.J., 2019. Facile construction of MoO_3@ZIF-8 core-shell nanorods for efficient photoreduction of aqueous Cr(VI). Appl. Catal. B Environ. 240, 92–101.

Zhao, H., Xia, Q., Xing, H., Chen, D., Wang, H., 2017. Construction of pillared-layer MOF as efficient visible-light photocatalysts for aqueous Cr(VI) reduction and dye degradation. ACS Sustain. Chem. Eng. 5, 4449–4456.

Zhou, W.J., Yin, Z.Y., Du, Y.P., Huang, X., Zeng, Z.Y., Fan, Z.X., Liu, H., W, J.Y., Zhang, H., 2013. Synthesis of few-layer MoS_2 nanosheet-coated TiO_2 nanobelt heterostructures for enhanced photocatalytic activities. Small 9, 140–147.